Active Wavefront Correction in Laser Interferometric Gravitational Wave Detectors Technical Notes v0.1 T010056-00-R

Ryan Lawrence
MIT LIGO Lab

May 1, 2001

1 Introduction

As the first generation of laser interferometric gravitational wave detectors near completion, research and development has begun on increasing the instrument's sensitivity while utilizing the existing infrastructure. In the Laser Interferometer Gravitational Wave Observatory (LIGO), incremental upgrades are being planned to occur within the next five years, improving strain sensitivity though active seismic isolation systems, lower loss optical materials, and higher input laser power. Even with the highest quality optics available today, however, finite absorption of laser power within transmissive optics, coupled with the tremendous amount of optical power circulating in various parts of the interferometer, result in critical wavefront deformations which will cripple the performance of the instrument.

This project seeks to develop an active wavefront compensation scheme via direct thermal actuation on the affected optics, while not degrading the instrument's length sensitivity of $\delta x \sim 10^{-21} m/\sqrt{Hz}$ at $100 Hz$. A simple nichrome heating element suspended off the face of an affected optic will, through radiative heating, remove the gross axisymmetric part of the original thermal distortion. A scanning heating laser (CO_2 laser, $\lambda = 10.6 \mu m$) will then be used to remove any remaining non-axisymmetric wavefront dis-

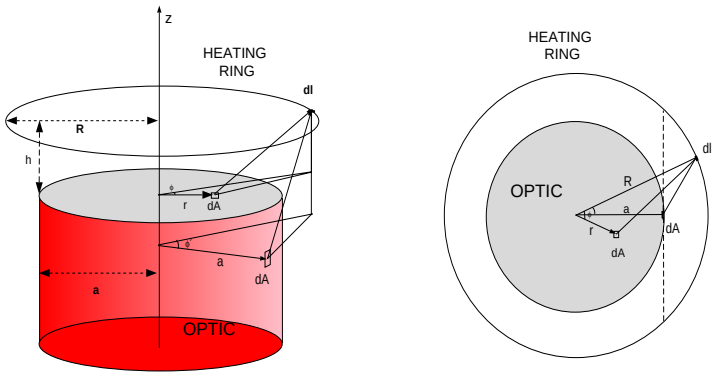

Figure 1: Diagram of the coordinates used in this paper.

tortion, generated by inhomogeneities in the substrate's absorption, thermal conductivity, etc. Careful attention must be paid to the intensity noise in both schemes, as these intensity fluctuations will couple directly into displacement noise.

2 Thermal effects in LIGO II

Insert general overview of the problem here...

2.1 Calculating Optical Path Length Changes

Given the temperature field $T(r,z)$ of the heated optic, the optical path length $\phi_t(r)$ for transmission can be approximated:

$$\phi_t(r) = \int_0^{h(r)} n(r,z)\,dz \tag{1}$$

$$\simeq n_0 h_0 + \frac{dn}{dT}\int_0^{h_0} (T(r,z) - T_\infty)\,dz + n_0(h(r) - h_0) \tag{2}$$

$$= \phi_{t0} + \phi_{tl}(r) + n_0 \Delta h(r) \tag{3}$$

Where h_0 is the nominal distance through the optic, n_0 is the nominal index of refraction of the substrate, $h(r)$ is the displacement of the surface due to thermal expansion at radius r, ϕ_{t0} is the nominal undistorted optical path through the optic, $\phi_{tl}(r)$ is the optical path distortion attributed to thermal lensing, and $\Delta h(r) \equiv h(r) - h_0$ is the thermoelastic deformation of the surface. For direct reflections off the affected face, the optical path length may be written:

$$\phi_r(r) = \phi_{r0} - 2\Delta h(r) \tag{4}$$

If we assume that the maximum temperature of the optic is small compared to the ambient temperature:

$$\frac{\max(T) - T_0}{T_0} \ll 1 \tag{5}$$

which is necessary in order to prevent the generation of additional thermal noise in the affected optic ($T_0 = 300°K$), then we may linearize the equations governing heat transfer in terms of $T - T_0$ (see Appendix A).

Using a finite element model to numerically solve the heat transfer equation determining $T(r,z)$, the optical path length change due to thermal lensing is calculated. The calculated temperature field may then be loaded into another finite element model for calculating the vector field of deformations, $\boldsymbol{u}(r,z)$, to obtain the surface deformation $\Delta h(r)$=$u_z(r, z = h_0)$ (see Appendix B).

In principle, solving the coupled partial differential equations for the thermoelastic deformation is computationally intensive compared to the calculation for the temperature field. A close (within a factor of 2) approximation for use in minimization can be made as:

$$\Delta h(r) \simeq \alpha \int_0^{h_0} (T(r,z) - T_\infty)\, dz = \beta \phi_{tl}(r)$$

where $\beta \equiv \alpha / \frac{dn}{dT}$, with α the thermal expansion coefficient.

2.2 Figure of Merit

If an initially pure TEM_{00} beam is acted on by a distorted optic (under either reflection or transmission), the beam suffers a radially dependent phase distortion, which we discussed in the previous sections in terms of the net optical path $\phi(r)$. In a modal representation (due to the cylindrical symmetry, we use the Laguerre-Gauss representation), the acquired phase distortion is equivalent to power being scattered out of the TEM_{00} beam and into higher order cylindrically symmetric modes. The fractional power lost out of the TEM_{00} mode, termed the "distortion parameter", is calculated as:

$$\begin{aligned} \mathcal{G} &= 1 - \left| < 00 | e^{i \frac{2\pi}{\lambda} \phi(r)} | 00 > \right|^2 \\ &= 1 - \frac{16}{w^4} \left| \int_0^\infty e^{i \frac{2\pi}{\lambda} \phi(r)}\, e^{-2 \frac{r^2}{w^2}}\, r\, dr \right|^2 \end{aligned}$$

To gauge the effectiveness of a given correction, we define the "correction parameter" $\mathcal{C} = \mathcal{G}_0 / \mathcal{G}$, with G_0 and G the uncorrected and corrected distortion parameters, respectively, to indicate the degree of wavefront correction. While not necessarily an acurrate gauge of the effects of wavefront distortions (or corrections) in an interferometric gravity wave detector, a vanishing value of $\mathcal{G}$ (hence a large value of $\mathcal{C}$) represents an ideal optical element. Thus, we will gauge the effectiveness of correction (or severity of distortion) by the value of the correction parameter.

2.3 Calculated Thermal Effects in LIGO II ITM's

Utilizing the physical parameters listed in Table (1), we may calculate the effects of absorbing a power P_{abs} in LIGO II test masses, due to absorption

of the interferometer's main beam. Figures 7 and 8 shows the resulting temperature fields, as well as calculated transmitted and reflected optical path distortions for both fused silica and sapphire for 1 Watt of absorbed power.

Material	Parameter	Value
Fused Silica	Thermal Conductivity	$\kappa = 0.0138$ W/cm/°K
	Index Derivative	$\frac{dn}{dT} = 11.8 \times 10^{-6}$/°K
	Expansion/Lensing Ratio	$\beta = 0.05$
	Heat Capacity	$c = 0.74$ J/g°K
	Density	$\rho = 2.20$ g/cm^3
Sapphire	Thermal Conductivity	$\kappa = 0.41$ W/cm/°K
	Index Derivative	$\frac{dn}{dT} = 12 \times 10^{-6}$/°K
	Expansion/Lensing Ratio	$\beta = 0.5$
	Heat Capacity	$c = 0.77$ J/g°K
	Density	$\rho = 3.98$ g/cm^3

Table 1: Material parameters assumed.

Figure (2) shows the calculated $\mathcal{G}_I$ vs. P_{abs} for reflected and transmitted beams in both sapphire and fused silica ITM's. It is instructive to note that, in LIGO I, with an input laser power of 8 Watts, a recycling gain of 30, and an arm cavity finesse of 200, the power absorbed in the fused silica input test masses will be $\sim$ 25mW, corresponding to a distortion parameter of $\sim 5 \times 10^{-3}$ in transmission, a level which is compensated for by adjusting the "cold curvature" of affected mirrors to facilitate the proper curvature under "hot" operation.

3 Static Thermal Compensation

One can construct a simple geometry of axisymmetric radiative heaters and reflectors to compensate anticipated axisymmetric thermal distortions. Changing the temperature of the electric heating elements via control of DC current allows the strength of the correction to be continuously altered.

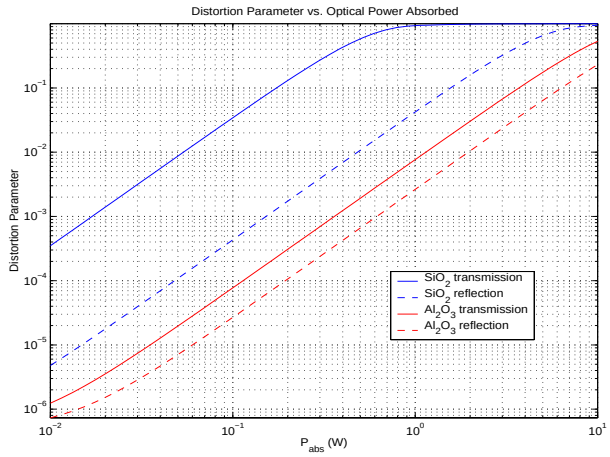

Figure 2: Fractional power scattered out of the TEM_{00}, mode of the interferometer's main beam, $\mathcal{G}_0$, for singe pass transmission (solid line) and single reflection (broken line) off of the arm cavity side of LIGO II input test masses of sapphire (red) and fused silica (blue).

3.1 Theory

The most simple geometry conceivable is a thin heating ring, mounted away from the face of the optic under actuation, centered on the optical axis (symmetry axis) with a radius larger than the optic's radius (to prevent unnecessary scattering out of the main LIGO beam). The radiation pattern of the simple heating ring of radius R, radiating power P, suspended a height h above the face of the optic is calculated to be (see figure (14) for a diagram):

$$H_s(r) = \frac{P\,h}{2\pi^3}\int_{-\pi}^{\pi}\frac{((R-r\cos\phi)^2+h^2)^{\frac{1}{2}}}{\left((R^2+r^2+h^2)-2Rr\cos\phi\right)^2}\,d\phi \tag{6}$$

Applying this boundary condition in the partial differential equation for temperature (equation (18) in Appendix A), the corresponding optical path length change, and hence the distortion parameter $\mathcal{G}(h,R,P)$, can be calculated and minimized against the predicted LIGO II distortion.

For a given absorbed power out of the main beam, P_{abs} we choose a fixed grid of ring positions, (h_i, R_j), and minimize $\mathcal{G}(h_i, R_j, P)$ over P. For clarity, we define a "ring power parameter", $\mathcal{P}$, as required ring power, per unit ring length, per unit absorbed power,(i.e. $P/2\pi R/P_{abs}$).

For fused silica, our simulations (see figures (9) and (10)) indicate that it is possible to achieve a correction which takes $\mathcal{C} \sim 10^2$ by placing the heating ring anywhere in a 1 cm wide band extending from $(R = 12.5cm, h = 4cm)$ to $(R = 16cm, h = 6cm)$, with a ring power parameter of $\sim 12.5cm^{-1}$. The corresponding maximal temperature increase of the optic, however, is seen to be $\sim 375°K$ per Watt of beam power absorbed. Thus, to keep the temperature increase at a level required to keep the heat transfer equation linear, as well as keeping added thermal noise to a minimum (equation (5)), the maximal absorbed power a single simple ring can compensate in fused silica is ~ 0.1 Watt.

For sapphire, due to the larger thermal conductivity, a correspondingly larger ring power is required to compensate a thermal lens of similar magnitude to that in fused silica (ring powers of order 1 kWatt would be required). Furthermore, sapphire is transmissive at wavelengths shorter than 5 microns, thus putting stringent limits on heater element temperature ($T_{comp} < 500°K$). A simple ring heater is thus deemed impractical for compensating sapphire.

One clear contributor to the inefficiency of the single heating ring is the fact that heat is deposited in the center of the optic, where heating which we are attempting to compensate occurs. One method of eliminating this spurious central heating is to include a cylindrical shield, with a radius equal to the optic's (thus smaller than the ring's), and a height such that the central portion of the optic is shielded from the ring's radiation. The calculation of the radiation pattern is identical for that of a simple ring, except the limits of integration in equation (6) are now dependent on r. For a ring of radius R and height h, shielded by a coaxial sheath of height h' and radius a, the limits $\phi_l(r)$ are found by numerically solving the equation:

$$\frac{a^2 + r^2 - 2ar\, f(\phi_l)}{R^2 + r^2 - 2rR\cos(\phi_l)} = \frac{h'}{h} \tag{7}$$

where $f(\phi_l)$ is calculated from:

$$f(\phi_l) \equiv \frac{rR^2}{a\rho^2}\sin^2(\phi_l)\left(1 \pm \left(1 - \frac{\rho^2}{R^2\sin^2(\phi_l)}\right)^{\frac{1}{2}}\left(1 - \frac{a^2}{r^2}\frac{\rho^2}{R^2\sin^2(\phi_l)}\right)^{\frac{1}{2}}\right)$$

with $\rho^2 \equiv R^2 + r^2 - 2rR\cos(\phi_l)$.

Yet another contributor to the inefficiency of the single heating ring is the dissipation of heat out the radial surface of the optic. Suspending an

aluminum sheath around this surface prevents radiation exchange with the thermal photon bath, hence reducing radial temperature gradients. The boundary condition on the edge of the optic (equation (18) in appendix A) is then $\frac{\partial T}{\partial r} = 0$.

For fused silica, our simulations (see figures (11) and (12)) of a shielded ring compensating an insulated optic indicate that it is possible to achieve corrections of order $\mathcal{C} \sim 10^3$ over a broad range of parameter values, while inducing a maximum temperature increase of $48°K$ per Watt of power absorbed. Furthermore, less ring power is required (the largest ring power parameter seen for a particular correction in this scheme is $\sim 9cm^{-1}$).

Due to the broad parameter space of the shielded ring compensating an insulated test mass, it is possible to obtain a modest correction in sapphire ($\mathcal{C} \sim 10^2$) with a ring power such that it is possible to maintain the relatively low temperature limit of $500°K$ (ring power parameter of $1.5cm^{-1}$). See figure (13).

3.2 Experiment

The sensing scheme we use to detect thermally induced optical path distortions utilizes a probe beam from a fiber pigtailed diode laser ($\lambda = 633$nm), coupled into a single mode fiber and collimated with a grin lens. The beam is expanded to the size of the optic under test, which is mounted in a high vacuum chamber. The reflected beam from transmission through the optic is sent back through the optical system, where is it picked off with a quarter-waveplate/polarizing beamsplitter and directed into a commercially available Shack-Hartmann wavefront sensor. Wavefront slopes relative to the initial "cold" wavefront are resolved over the sensor's 44×33 lenslet grid, and the resulting optical path distortion is reconstructed over the clear aperture. See figure (14) for a diagram of the sensing scheme.

To test the concept of the shielded ring with an insulated optic, a shielded ring was constructed and installed in vacuum. See figure (15) for a photograph and schematic. At $t = 0$, a total power of 10 Watts is supplied to the ring, and the resulting optical path distortion is measured. Linearly interpolating the measured optical path distortion to a polar grid over the aperture, and averaging over the angular coordinate, we obtain the optical path distortion as a function of radius, $\phi_{tl}(r)$. Figure (16) shows $\phi_{tl}(r)$ at the optic's edge, and at $r = 25$mm, as well as the results predicted by the finite element model we have constructed with equations (6) and (7). The thermal

time constant of the heating element after initial switch-on is included in the model.

4 Dynamic Thermal Compensation

It is possible to remove non-axisymmetric wavefront distortions through an optic by utilizing a well absorbed laser beam, modulated and scanned over a single face of an affected optic. By tailoring the power deposited in over a discrete, constant scanning pattern, one can generate an arbitrary wavefront distortion/correction.

4.1 Theory

Given a phase map $\phi(r, \theta)$, it may be decomposed into a representation of N nondegenerate functions Z_n (Hermite-Gauss, Laguerre-Gauss, Zernike, etc.), where N is determined by the degree of accuracy we require:

$$\phi(r, \theta) = \sum_{1}^{N} A_n Z_n(r, \theta)$$

or, in vector form:

$$\phi(r, \theta) = \vec{A} \cdot \vec{Z}(r, \theta)$$

If we wish to induce the phase map ϕ, we must find the required laser power over the constant scanning pattern. Suppose the scanning pattern shines the correcting Gaussian laser beam of waist w_a:

$$I(\vec{r}) = \frac{2P_m}{\pi w_a^2} e^{-2\frac{(\vec{r}-\vec{r}_m)^2}{w_a^2}}$$

over a discrete grid containing M points, indexed by m. We wish to find the M-dimensional "power vector" $\vec{P}$ to induce the N dimensional phase decomposition $\vec{A}$. To do this, we numerically find the "actuation operator" $\underline{O}$ (an $M \times N$ matrix) such that $\vec{P} = \underline{O} \cdot \vec{A}$.

Shining the actuation laser of unit power on the mth grid point results in a steady state phase distortion (either measured or numerically calculated) ϕ_m, which may be decomposed into our set of orthonormal functions, $\phi_m = \sum_1^N a_{nm} Z_n$. Doing this for all M grid points, the coefficients a_{nm} compose an

operator (an $N \times M$ matrix) $\underline{a}$ which allows us to determine the wavefront distortion $\vec{A}$, given a power vector $\vec{P}$:

$$\vec{A} = \underline{a} \cdot \vec{P}$$

Clearly, the actuation operator $\underline{O}$ is identical to the inverse of the matrix $\underline{a}$

So, given a measured wavefront distortion $\phi(r, \theta)$, in order to restore the measured wavefront to flat, we need to utilize the scanning laser to induce an additional wavefront curvature $\phi_c(r, \theta) = C - \phi(r, \theta)$, where C is an arbitrary constant over (r, θ) chosen to minimize the necessary correcting laser power (and keep it a positive value for all grid points m). Decomposing $\phi_c(r, \theta)$ into components A_n, we calculate the desired correcting power vector $\vec{P}$ as

$$\vec{P} = \underline{O} \cdot \vec{A}.$$

4.1.1 Using Zernike Polynomials

4.1.2 Using Actuation Functions

We define the actuation function $\mathcal{A}_l(r, \theta)$ as the steady-state wavefront distortion over the entire aperture generated by the actuating beam shining on the lth actuation point (r_l, θ_l), in units of length per unit energy. All correctible wavefront distortions for a given scan pattern may be expressed as:

$$\phi(r, \theta) = \sum_{n=1}^{N} P_n \mathcal{A}_n(r, \theta)$$

where N is the total number of actuation points, and P_n is the beam power deposited on the nth actuation point.

Given wavefront data ϕ_l over a set of M discrete points (x_l, y_l) we construct a merit funtion:

$$\chi^2 = \sum_{l=1}^{M} (\phi_l + C - \phi_{\text{fit}}(x_l, y_l))^2$$

where C is an arbitrary constant with units of length and:

$$\phi_{\text{fit}}(x_l, y_l) \equiv \sum_{n=1}^{N} P_n \mathcal{A}_n(x_l, y_l)$$

as before. Minimizing the merit function gives us the best possible correction for a measured distortion in a given actuation basis. We may solve this problem using matrix methods.

Differentiating the merit function with respect to P_n and equating to zero, we get a set of N equations:

$$\begin{aligned} 0 &= \sum_{m=1}^{N} P_m \sum_{l=1}^{M} \mathcal{A}_m(x_l, y_l)\mathcal{A}_n(x_l, y_l) - \sum_{l=1}^{M} \phi_l(\mathcal{A}_n(x_l, y_l) + C) \\ &= \sum_{m=1}^{N} P_m A_{n,m} - d_n \end{aligned}$$

where we have defined:

$$d_n \equiv \textstyle\sum_{l=1}^{M} \phi_l(\mathcal{A}_n(x_l, y_l) + C) \qquad A_{n,m} \equiv \textstyle\sum_{l=1}^{M} \mathcal{A}_n(x_l, y_l)\mathcal{A}_m(x_l, y_l).$$

which is equivalent to the matrix equation:

$$\vec{d} = \underline{A} \cdot \vec{P}$$

The N dimensional power vector is now found by inverting the $N \times N$ matrix A:

$$\vec{P} = \underline{A}^{-1} \cdot \vec{d} \tag{8}$$

Given wavefront slope data $(\partial_x\phi_l, \partial_y\phi_l)$ over a set of M discrete points (x_l, y_l), as is the case of a Shack-Hartmann sensor, we construct the merit function:

$$\chi^2 = \sum_{l=1}^{M} \left[\left(\partial_x\phi_l + C_x - \partial_x\phi_{\text{fit}}(x_l, y_l)\right)^2 + \left(\partial_y\phi_l + C_y - \partial_y\phi_{\text{fit}}(x_l, y_l)\right)^2 \right]$$

where C_x and C_y are arbitrary dimensionless constants, and:

$$\partial_x\phi_{\text{fit}}(x_l, y_l) \equiv \sum_{n=1}^{N} P_n \partial_x \mathcal{A}_n(x_l, y_l)$$

with a similar result for the y-direction terms. Organizing to form the matrix equation (8), we find the matrix elements to be:

$$d_n \equiv \sum_{l=1}^{M} [\partial_x \phi_l (\partial_x \mathcal{A}_n(x_l, y_l) + C_x) + \partial_y \phi_l (\partial_y \mathcal{A}_n(x_l, y_l) + C_y)]$$

$$A_{n,m} \equiv \sum_{l=1}^{M} [\partial_x \mathcal{A}_n(x_l, y_l) \partial_x \mathcal{A}_m(x_l, y_l) + \partial_y \mathcal{A}_n(x_l, y_l) \partial_y \mathcal{A}_m(x_l, y_l).]$$

We are then able to determine $\vec{P}$ via equation (8).

4.2 Experiment

The sensing scheme is identical to that described in Section (3.2) and Figure (14). Here, however, a scanning laser beam is utilized instead of the heating ring. The galvanometer scanners are driven over a constant polar pattern (each galvanometer is driven sinusoidally with a linearly increasing/decreasing amplitude). Wavefront data are periodically read (once per e-folding time of the optic under actuation) from the Shack-Hartman sensor, the necessary actuation powers are calculated from the measured wavefront decomposition, and are then implemented via acousto-optic modulation of the CO_2 beam. Construction and calibration of the apparatus has begun, with the first full test planned for February, 2001.

5 Noise Considerations

By virtue of the fact that our actuation schemes actively alter the optical path length through different components of the interferometer, unchecked intensity fluctuations of the heating source in either actuation scheme will couple directly into displacement noise.

We may calculate the frequency response of the optical path through an optic due to an oscillating source of the form: $I(r, \phi, \omega t) = R(r, \phi) \exp(-i\omega t)$. where we have removed the DC component of the source. Let a be the characteristic width of the spatial pattern $R(r)$. If $\frac{2\pi}{\omega}$ is much smaller than the local time constant of the optic, $\tau_l \simeq \frac{a^2 \rho c}{k}$, which is $\sim$ 10s for $a = 1$cm on a sapphire optic, then we may neglect radial diffusion of absorbed energy.

The energy per unit area contained in a column through the optic is then given by:

$$E(r, \phi, \omega t) = \frac{-1}{i\omega} I(r, \phi, \omega t)$$

However, if the temperature field is known, the energy per unit area in the column can be calculated as:

$$E(r, \phi, \omega t) = \rho c \int_0^H T(r, \phi, z, t)\, dz$$

Equating the previous two equations, we get:

$$\int_0^H T(r, \phi, z, t)\, dz = \frac{i}{\rho c \omega} I(r, \phi, \omega t)$$

The surface of the affected optic will then deform by an amount:

$$\delta x_s(r, \phi, \omega t) \simeq \frac{\alpha i}{\rho c \omega} I(r, \phi, \omega t)$$

and the optical path through the optic will change by:

$$\delta x_t(r, \omega t) \simeq \frac{(\alpha + \frac{dn}{dT}) i}{\rho c \omega} I(r, \phi, \omega t)$$

Given the target sensitivity of the instrument and the surface of actuation (recycling cavity vs. arm cavity), this calculation puts an upper limit on the tolerable intensity noise of thermal actuators, $I(r, \phi, \omega)$. If the surfaces of the arm cavity are actuated, then the measured change in arm length is simply:

$$\delta x_{\rm arm}(\omega t) = \frac{2}{\pi w^2} \frac{\alpha i}{\rho c \omega} \exp(i\omega t) \int_0^\infty \int_0^{2\pi} e^{-2\frac{r^2}{w^2}} I(r, \phi, \omega) r\, dr\, d\phi \qquad (9)$$

where w is the waist of the LIGO beam at the optic under actuation. If, instead, the surfaces within the recycling cavity are actuated, where the interferometer's sensitivity to length changes is diminished by the finesse of the arm cavity F (~ 200), then intensity noise in the actuator will create a resulting noise in the measured arm length $\delta x_{\rm rc} = \frac{1}{F} \delta x_{\rm arm}$.

For example, consider the so-called "photo-thermal noise", generated by shot noise in absorbed (i.e. detected) laser light on the Fabry-Perot surface

of a test mass. With an arm cavity power of $P_{\rm arm}$ and a surface absorption of α_s, the total intensity fluctuation due to shot noise alone is given by:

$$\Delta P = \sqrt{2\epsilon\alpha_s P_{\rm arm}}$$

where ϵ is the energy of a single arm cavity photon. So, plugging the fluctuation function given by:

$$I(r,\phi,\omega) = \frac{2\Delta P}{\pi w^2} e^{-2\frac{r^2}{w^2}}$$

into equation (9), we get a measured amplitude of length fluctuation:

$$|\delta x_{\rm arm}| = \frac{\alpha\sqrt{2\epsilon\alpha_s P_{\rm arm}}}{\pi w^2 \rho c \omega}$$

For $P_{arm} = 830$ kW, $\alpha_s = 0.5$ppm, $w = 3.65$cm, and the parameters listed for sapphire in table (1), this yields a measured arm cavity length fluctuation (for a single mirror fluctuating) of amplitude:

$$|\delta x_{\rm arm}| = 2 \times 10^{-21}{\rm m}/\sqrt{\rm Hz}$$

at $\omega = 100$Hz.

5.1 Noise from a Laser Actuator

At a given instant, the actuator beam will be depositing energy at a pattern point $\vec{r_0} = (x_0, y_0)$, and we may write the intensity noise of this beam as:

$$I(x,y,\omega) = \frac{2\Delta P(\omega)}{\pi w_a^2} e^{-2\frac{(x-x_0)^2+(y-y_0)^2}{w_a^2}}$$

where w_a is the waist of the beam and ΔP is the spectral density of the beam power at frequency ω. Without loss of generality, we may set $y_0 = 0$, $x_0 = r_0$. We may now use equation (9) to calculate the upper limit required on $\Delta P(\omega)$ as a function of the actuation radius r_0.

Figure (3) shows the power fluctuations ΔP required in a correcting beam with $w_a = 1$cm to induce length fluctuations of $|\delta x| = 10^{-20}{\rm m}/\sqrt{\rm Hz}$ as a function of actuation radius r_0 at a frequency of $\omega = 100$Hz. As before, we use $w = 3.65$cm for the main beam size.

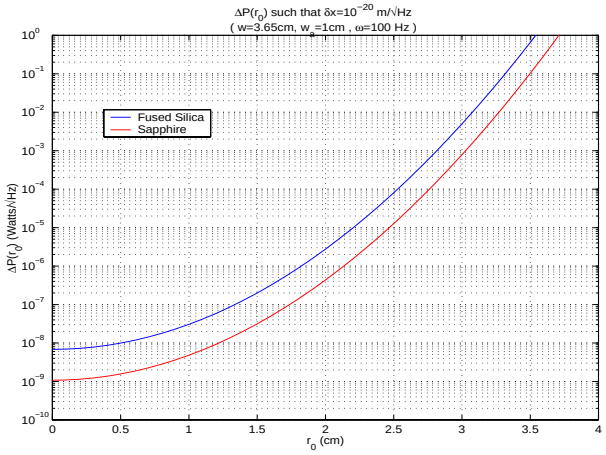

Figure 3: Power fluctuations in an actuating beam of size $w_a = 1$cm, shining at radius r_0 off of the main optical axis, that will induce measured length fluctuation $\delta x = 10^{-20}\mathrm{m}/\sqrt{\mathrm{Hz}}$, with a main beam waist of $w = 3.65$cm.

5.2 Noise From a Blackbody Actuator

It is well known [4] that the root mean square fluctuation in photon number $\Delta n_{\omega 0}$ for a single field mode in an ideal blackbody source is given by:

$$\Delta n_{\omega 0} = \sqrt{\bar{n}_{\omega 0}^2 + \bar{n}_{\omega 0}}$$

where n is the mean photon number in the mode, given by the Planck thermal excitation function $\bar{n}_{\omega 0} = 1/(e^{\frac{hc}{\lambda k T}} - 1)$. Clearly, for $\bar{n}_{\omega 0} > 1$, the fluctuations are approximately equal to the mean number of photons in the mode, while for $\bar{n}_{\omega 0} < 1$ the statistics become Poissonian. The wavelength where $\bar{n}_{\omega 0} = 1$ is easily calculated to obey the relation:

$$\lambda_c T = 0.02\,\mathrm{m}\,^{\circ}\mathrm{K}.$$

Utilizing Wien's displacement law, $\lambda_{\max} T = 0.003$ m°K, we get the quite general relation:

$$\frac{\lambda_c}{\lambda_{\max}} = 6.67.$$

Using this result, and integrating the blackbody energy density, it can be easily shown that 1.6% of the total radiated energy resides in the non-Poissonian tail.

In a realistic blackbody source, the effect of spatial extent of the source must be taken into account to properly calculate the total statistical fluctuation. The coherence length of the emitted light, l_c, (approximately equal to the wavelength of the mode for blackbody light) defines the scale of coherence between spatially separated radiators. Light emitted from separated "coherence patches" (patches of area l_c^2) will thus be statistically independent. An identical argument applies to the "detector" (the face of the optic under actuation), since radiation from a single coherence patch arriving at spatially separated positions of the optic will be uncorrelated if the difference in travel time is longer than the coherence time $t_c = l_c/c$. For N_c coherence patches (detector plus radiator), the mean photon number in a given field mode becomes $\bar{n}_\omega = N_c \bar{n}_{\omega 0}$. Similarly, the root mean square is $(\Delta n_\omega)^2 = N_c(\Delta n_{\omega 0})^2$, thus yielding:

$$\frac{\Delta n_\omega}{n_\omega} = \frac{\sqrt{N_c(\bar{n}_{\omega 0}^2 + \bar{n}_{\omega 0})}}{N_c \bar{n}_{\omega 0}} \tag{10}$$

$$= \sqrt{\frac{1}{N_c} + \frac{1}{\bar{n}_\omega}}. \tag{11}$$

Note that for $\bar{n}_\omega < N_c$, the fractional photon fluctuation is closely Poissonian, while it is a constant $1/N_c$ otherwise. The new λ_c (where $\bar{n}_\omega = N_c$) is calculated to be:

$$\frac{\lambda_c}{\lambda_{\max}} = 6.67 \times \log(N_c + 1). \tag{12}$$

Since $N_c = A/l_c^2$ depends on the coherence length $l_c \sim \lambda_c$, this equation becomes transcendental in λ_c. We are forced to numerically solve for λ_c given area emitter/detector area A and emitter temperature T.

For our radiator/detector system, the typical peak wavelength is $\lambda_{max} \simeq 7\mu$m, with a total detector/emitter area of $A \simeq 0.05\text{m}^2$. Solving equation (12) for λ_c, we find the number of disjoint (statistically independent) coherence patches to be $N_c \sim 1 \times 10^5$, which results in 0.0013% of the total emitted power in the non-Poissonian tail. Thus, for the geometry and wavelengths we are concerned with, the counting statistics on radiated photons may be considered purely Poissonian.

More to come...

6 Measuring Material Parameters

In the course of the previous tests, it was realized that material parameters (e.g. thermal conductivity) could be accurately extracted with little modification to the existing setup. Assuming the axisymmetric thermal model to be correct, measuring the step response of the peak-to-valley optical path to the heating laser beam places tight constraints on the thermal conductivity, index derivative, and thermal expansion coefficient. Tests have been performed on both fused silica and sapphire test pieces.

6.1 Calculations

We illuminate the optic under test with a CO_2 laser beam ($\lambda = 10.6\mu$m) of power P and waist w, so that the source terms in equations 17 and 18 become:

$$H_b(r,z,t) = 0 \qquad H_s(r,z=h,t) = \begin{cases} 0, & \text{for } t < 0; \\ \frac{2P}{\pi w^2} e^{-2\frac{r^2}{w^2}}, & \text{otherwise.} \end{cases} \tag{13}$$

The total optical path length through an optical element may be written as:

$$\begin{aligned} \phi(r) &= \int_0^{h(r)} n(r,z)\, dz \\ &\simeq n_0 h_0 + \frac{dn}{dT} \int_0^{h_0} (T(r,z) - T_\infty)\, dz + n_0(h(r) - h_0) \\ &= \phi_0 + \phi_l(r) + \phi_d(r) \end{aligned}$$

where h_0 is the nominal distance through the optic, $h(r)$ is the distance through the optic at radius r under thermoelastic deformation, ϕ_0 is the nominal undistorted optical path through the optic, $\phi_l(r,t)$ is the optical path distortion attributed to thermal lensing, and $\phi_d(r,t)$ is the optical path distortion due to thermoelastic deformation.

One quantity of interest is the peak-to valley optical path distortion generated by transmission into and the subsequent reflection through the test

optic. We may write this as:

$$\phi_{PV}(t) = 2P\left[\frac{dn}{dT}\int_0^h (T(z,0) - T(z,R))\,dz\right] + 2Pn\left[u_z(h,0) - u_z(h,R)\right] - 2P(n-1)\left[u_z(0,0) - u_z(0,R)\right] \quad (14)$$

where $T(z,r)$ is the temperature field, $u_z(z,r)$ is the resulting thermal deformation field in the z direction, n is the index of refraction, and $\phi_{PV}(t)$ is the measured peak to valley optical path distortion over the aperture of radius R.

The model is constructed by numerically solving the differential equations governing temperature and expansion. It is, however, straightforward to extract the functional dependence on the material parameters of interest from the analytic equations, thus minimizing the computation required to interpret the data.

It can be seen from equations (17) and (18) that:

$$T(r,z,t) = \frac{1}{k}\mathcal{T}(r,z,\beta t) \quad (15)$$

where $\beta \equiv \frac{k}{c\rho}$, and the function $\mathcal{T}(r,z,t)$ is independent of k, c, and ρ. Thus, the first term in equation (14) may be written as:

$$\frac{dn}{dT}\int_0^h \left[T(z,0) - T(z,R)\right]\,dz = A_{tl}f(\beta t)$$

where $A_{tl} \equiv \frac{dn}{dT}/k$ and the function $f(t)$ is independent of $\frac{dn}{dT}$, c, and k.

The equations governing thermoelastic deformations are considerably more complicated, so we leave the mathematical details to Appendix B. Using equation (15) in the thermoelastic equations of Appendix B, we see that the thermal expansion field u_z may be written:

$$u_z(r,z,t) = \frac{\alpha_z}{k}\mathcal{U}_{zr}(r,z,\beta t) + \frac{\alpha_r}{k}\mathcal{U}_{zz}(r,z,\beta t)$$

where $\mathcal{U}_{zr}$ is the z component of deformation which solves the thermal expansion equation with $\alpha_z = 0$ (the component of axial expansion generated by radial thermal expansion coupling into the axial direction via the Poisson

ratio), $\mathcal{U}_{zz}$ solves it for $\alpha_r = 0$ (the component of axial expansion due to axial thermal expansion), and both are independent of k, c, ρ, α_z, and α_r.

In the end, we write the total measured optical path distortion as:

$$\phi_{PV}(t) = A_{tl} f(\beta t) + A_z g_z(\beta t) + A_r g_r(\beta t) \tag{16}$$

$$A_{tl} \equiv \frac{dn}{dT}/k \qquad A_z \equiv \frac{\alpha_z}{k}$$
$$A_r \equiv \frac{\alpha_r}{k} \qquad \beta \equiv \frac{k}{c\rho}$$

where f, g_z, and g_r are numerically calculated functions, which are independent of the material parameters we wish to find. Figure (4) shows the fitting functions determined for the experiment's geometry. With the geometry under test, we find that f and g_z are nearly degenerate (i.e. we may find contants A and B such that $f(t) \simeq A g_z(Bt)$), and the magnitude of g_r is small compared to f and g_z. Thus, we can only realistically fit two of the four parameters to the data (β and one of the A's), and must assume knowledge of the other two.

6.2 Measurements

The sensing setup is identical to that of section 3.2, see figure (14) for a diagram. A shutter is placed in the heating beam, and triggered by the data acquisition routine, which subsequently triggers the Shack-Hartmann sensor in 0.5 second increments. The laser is intensity stabilized using a thermopile sensor, and the power is monitored over each data run.

6.3 Systematic Parameters

The parameters necessary to completely construct the fitting functions f, g_z, and g_r are the boundaries of the partial differential equation (the test optic's dimensions), the conditions on those boundaries (pump beam size, a, and the material's emissivity, ϵ), and the aperture sensed. If the pump beam size is much smaller than the physical dimensions of the test optic, then the fitting functions approach those for an infinite half space, hence depend

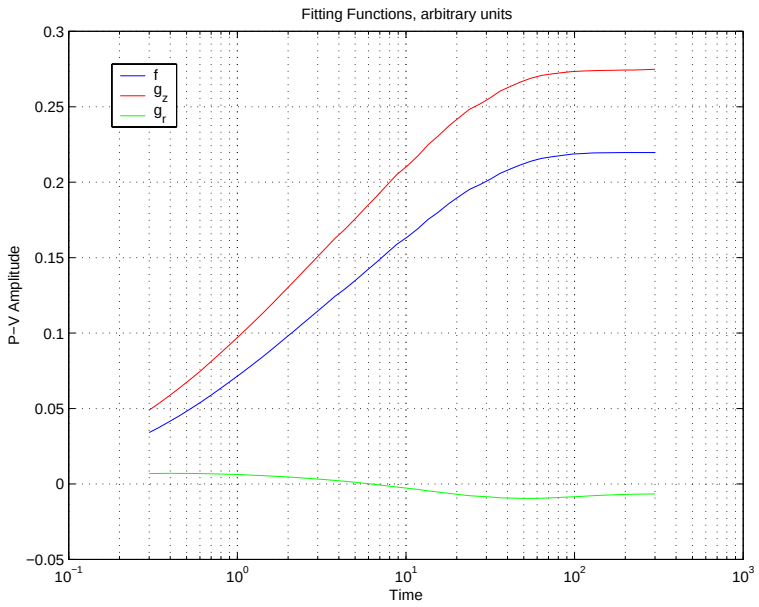

Figure 4: Numerically determined fitting functions f, g_z, and g_r for the geometry of the experiment.

very weakly on the physical dimensions of the optic and the emissivity of the radial surface. If the aperture sensed is also much larger than the beam size, then the peak-to-valley optical path distortion also very weakly depends on the aperture size (temperature gradients, hence optical path distortion effects, are localized to the region illuminated by the pump beam). We measure the optic's dimensions with a set of calipers, and simplify the radial surface's boundary conditions by wrapping it in a single layer of aluminum foil (emissivity ~ 0.1 at room temperature).

The emissivity of the face under test (at 10.6μm) determines the fraction of the pump beam which is absorbed on the surface under test. This is determined by measuring the fractional power of the pump beam which is reflected off of the face of the optic.

The effective local time constant (the time it takes for steady-state temperature gradients, hence optical path distortions, to form) is given by $\tau_l = \frac{\rho c}{k} a^2$. Uncertainty in a couples very strongly into the effective rise time of f, g_z, and g_r. From the expression for the local time constant, we see that the error in our measure of a (δa) propagates into the error for β as $2\frac{\delta a}{a}$.

We determine the size of the CO2 beam by measuring the power transmitted through an aperture of well-known size placed at the position of the optic's face when under test. The total pump power transmitted through the optical system is measured at the position of the optic under test (in the vacuum chamber at atmosphere) versus the power measured on the on-table power monitor. An aperture of well-known size is placed in front of the in-tank meter, the beam centration is adjusted to maximize the power registered, and the resulting in-tank power is measured versus the on-table power monitored. This is done for three aperture diameters (1 mm, 2.77 mm, and 6.73 mm), the results for each aperture are averaged, and the model (transmission for a pure Gaussian beam) is fit to the data in a least-squares fashion.

The spatial profile of the beam is measured by using galvanometers to scan in a grid pattern (100×100) over a 150μm pinhole placed in front of a pyroelectric sensor. The beam is chopped at 400Hz, the signal from the pyroelectric sensor (after a FET preamp) is sent to a lock-in amplifier, and the resultant signal is recorded by the computer which is controlling the scan pattern of the galvos. See figure (5) for an intensity map of the pump beam as a function of galvanometer voltage.

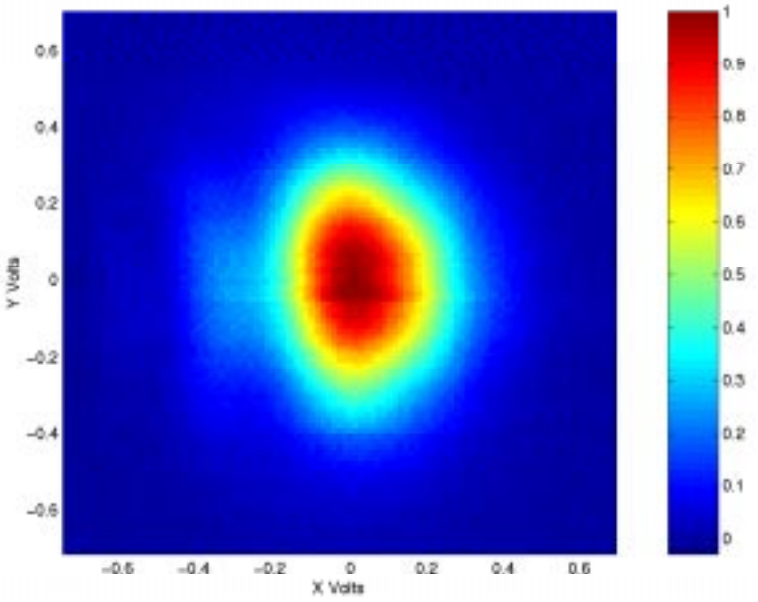

Figure 5: Measured spatial profile of the pump beam at the test optic.

Parameter	Value	Error
Beam Radius	5.01 mm	± 0.04 mm
Aperture	3.9 cm	± 0.1 cm
Fused Silica Emissivity	0.95	± 0.01
Sapphire Emissivity	0.89	± 0.02

Table 2: Systematic parameters and their errors.

6.4 Data

Figure (17) shows the peak to valley optical path distortion data. The data are normalized to measured absorbed power (pump power in the vacuum tank times measured emissivity), and averaged over multiple data runs. In the sapphire plot, the magenta triangles denote the statistical error on the average at each time.

7 Conclusions

Material parameters fit for fused silica are listed in table (3). If we assume standard values[2] for heat capacity ($c = 0.74$ J/g/°K) and density (2.2 g/cm^3), then this yields:

$$k = (1.25 \pm 0.07)\,\mathrm{W/m/^\circ K}$$
$$\frac{dn}{dT} = (8.9 \pm 0.10) \times 10^{-6}/^\circ\mathrm{K}$$

Parameter	Value	Error
A_{tl}	$7.14\,\mu$m/W	$\pm 0.086\,\mu$m/W
β	0.00768 cm^2/s	± 0.00042 cm^2/s

Table 3: Material parameters fit for fused silica.

Assuming known values of $\frac{dn}{dT} = 1.26 \times 10^{-5}/^\circ$K [3], $c = 0.775$ J/g/°K [2],

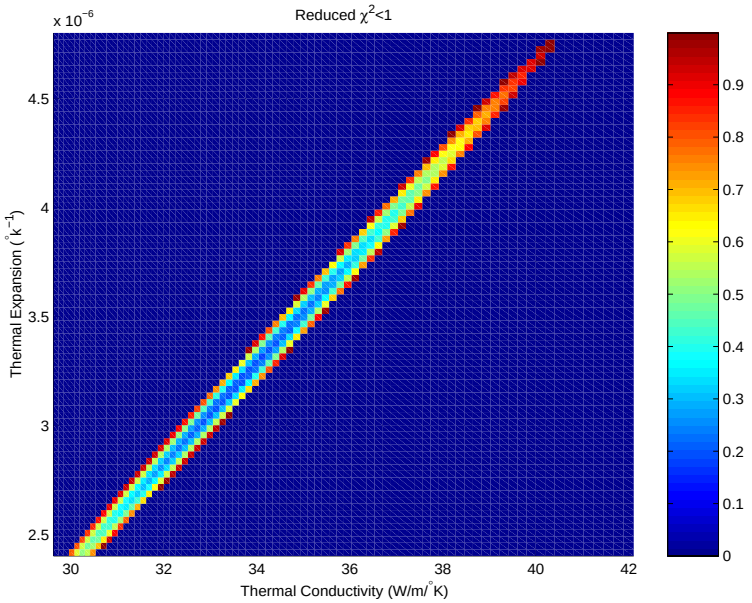

Figure 6: Reduced χ^2 as a function of thermal conductivity and thermal expansion assuming $c = 0.775$ J/g/°, $\rho = 3.98$ g/cm^3, and $\frac{dn}{dT} = 1.26 \times 10^{-5}$/°K. For clarity, values of $\chi^2 > 1$ are excluded.

and $\rho = 3.98$ g/cm^3 [2] we fit:

$$k = (33.8 \pm 4.0)\,\mathrm{W/m/^\circ K}$$
$$\alpha_z = (3.2 \pm 1.0) \times 10^{-6}/^\circ\mathrm{K}$$

The relatively large error bars on these fits is due to the degeneracy between f and g_z. See figure (6) for the reduced χ^2 versus k and α.

8 Conclusions

	$\mathcal{C}$	$\max(P_{abs})$	Notes
Bare Ring	1×10^2	100 mW	Steep Parameter Space
Shielded Ring, Insulated Optic	2×10^3	800 mW	Broad, Flat Parameter Space
Scanning Beam (Antigaussian)	1×10^5	1W	More Detailed Modeling Required

Table 4: Results of the finite element simulations for thermally compensating fused silica test masses.

	$\mathcal{C}$	$\max(P_{abs})$	Notes
Bare Ring	-	-	Impractical Due to Ring Power Required
Shielded Ring, Insulated Optic	1×10^2	1 W	Limited By Ring Power Required
Scanning Beam (Antigaussian)	-	-	Impractical Due to Laser Intensity Noise (?)

Table 5: Results of the finite element simulations for thermally compensating sapphire test masses.

A Calculating Temperature

The heat transfer equation for an arbitrary body in 3 dimensions is given by the Fourier equation:

$$\rho c \frac{\partial T(\vec{r},t)}{\partial t} - \vec{\nabla} \cdot (\underline{K} \vec{\nabla} T(\vec{r},t)) = H_b(\vec{r},t)$$

Where c is the heat capacity, ρ is the density, $\underline{K}$ is the thermal conductivity (a 3×3 matrix), T is the local temperature, and H_b is the rate of internal (bulk) heating due to an external source. If the body interacts only with a thermal radiation bath of temperature T_∞ (i.e. it is suspended in a vacuum enclosure with walls at termperature T_∞), the boundary equations are given by the Stefan-Boltzmann law:

$$\hat{n} \cdot (\underline{K} \vec{\nabla} T) = -\sigma \epsilon (T - T_\infty)^4 + H_s(\vec{r},t)$$

Where $\hat{n}$ is the unit normal on the surface, ϵ is the emissivity, σ is the Stefan-Boltzmann constant, and H_s is the rate of surface heating due to an external source. If we assume that $\frac{T-T_\infty}{T_\infty} \ll 1$, we may linearize the boundary conditions so that:

$$\hat{n} \cdot (\underline{K} \vec{\nabla} T) = -4\sigma \epsilon T_\infty^3 (T - T_\infty) + H_s(\vec{r},t)$$

Assuming cylindrical symmetry, the Fourier equation (A) may be reduced to two dimensional parabolic form:

$$\rho r c \frac{\partial T(r,z,t)}{\partial t} - \vec{\nabla_2} \cdot (\underline{k} r \vec{\nabla_2} T(r,z,t)) = r H_b(r,z,t) \tag{17}$$

With boundary conditions:

$$\hat{n} \cdot (\underline{k} r \vec{\nabla} T) = -4\sigma r \epsilon T_\infty^3 (T - T_\infty) + r H_s(\vec{r},t) \tag{18}$$

Where we have written $\vec{\nabla_2} \equiv \hat{r}\frac{\partial}{\partial r} + \hat{z}\frac{\partial}{\partial z}$, and $\underline{k}$ is now a 2×2 matrix.

Given the heating terms H_b and H_s, these equations may be solved numerically over a given two dimensional region using a parabolic finite element solver.

B Calculating Thermal Expansion

Given the stress temperature modulus $\vec{\gamma} = \gamma_z \hat{z} + \gamma_r \hat{r}$, shear modulus G, 1st Lame' coefficient μ, and the temperature field T of the object under test, the thermal deformation of the object can be numerically calculated. With a sufficient change of variables, the equations determining the thermal deformations $\boldsymbol{u} = \binom{u_r}{u_z}$ may be reduced to the form of a two dimensional elliptic system of partial differential equations, which, given any temperature field, can be solved over a two dimensional region using an elliptic finite element solver:

$$-\vec{\nabla} \cdot \left(\underline{\boldsymbol{c}} \otimes \vec{\nabla} \boldsymbol{u'} \right) = \boldsymbol{f} \tag{19}$$

Where $\boldsymbol{u'} \equiv \binom{ru_r}{u_z}$, $\boldsymbol{f}$ are volume forces generated by the temperature field $T(r, z, t)$, given by:

$$\boldsymbol{f} = \begin{pmatrix} \gamma_r \frac{\partial T}{\partial r} \\ \gamma_z r \frac{\partial T}{\partial z} \end{pmatrix}$$

and $\underline{\boldsymbol{c}}$ is a rank four tensor with elements:

$$\underline{c}_{11} = \begin{pmatrix} \frac{2G+\mu}{r} & 0 \\ 0 & \frac{G}{r} \end{pmatrix} \qquad \underline{c}_{12} = \begin{pmatrix} 0 & \mu \\ G & 0 \end{pmatrix}$$
$$\underline{c}_{21} = \begin{pmatrix} 0 & G \\ \mu & 0 \end{pmatrix} \qquad \underline{c}_{22} = \begin{pmatrix} Gr & 0 \\ 0 & (2G+\mu)r \end{pmatrix}$$

On the boundaries of the optic, stress in the direction of the normal must vanish. In our two dimensional framework, this is found to be equivalent to a generalized Neumann condition of the form:

$$\vec{n} \cdot \left(\underline{\boldsymbol{c}} \otimes \vec{\nabla} \boldsymbol{u'} \right) + \underline{q} \boldsymbol{u'} = \boldsymbol{g} \tag{20}$$

Where we have:

$$\underline{q} = \begin{pmatrix} -\frac{2G}{r^2} n_r & 0 \\ 0 & 0 \end{pmatrix} \qquad \boldsymbol{g} = \begin{pmatrix} \gamma_r n_r T \\ \gamma_z n_z r T \end{pmatrix}$$

C Figures

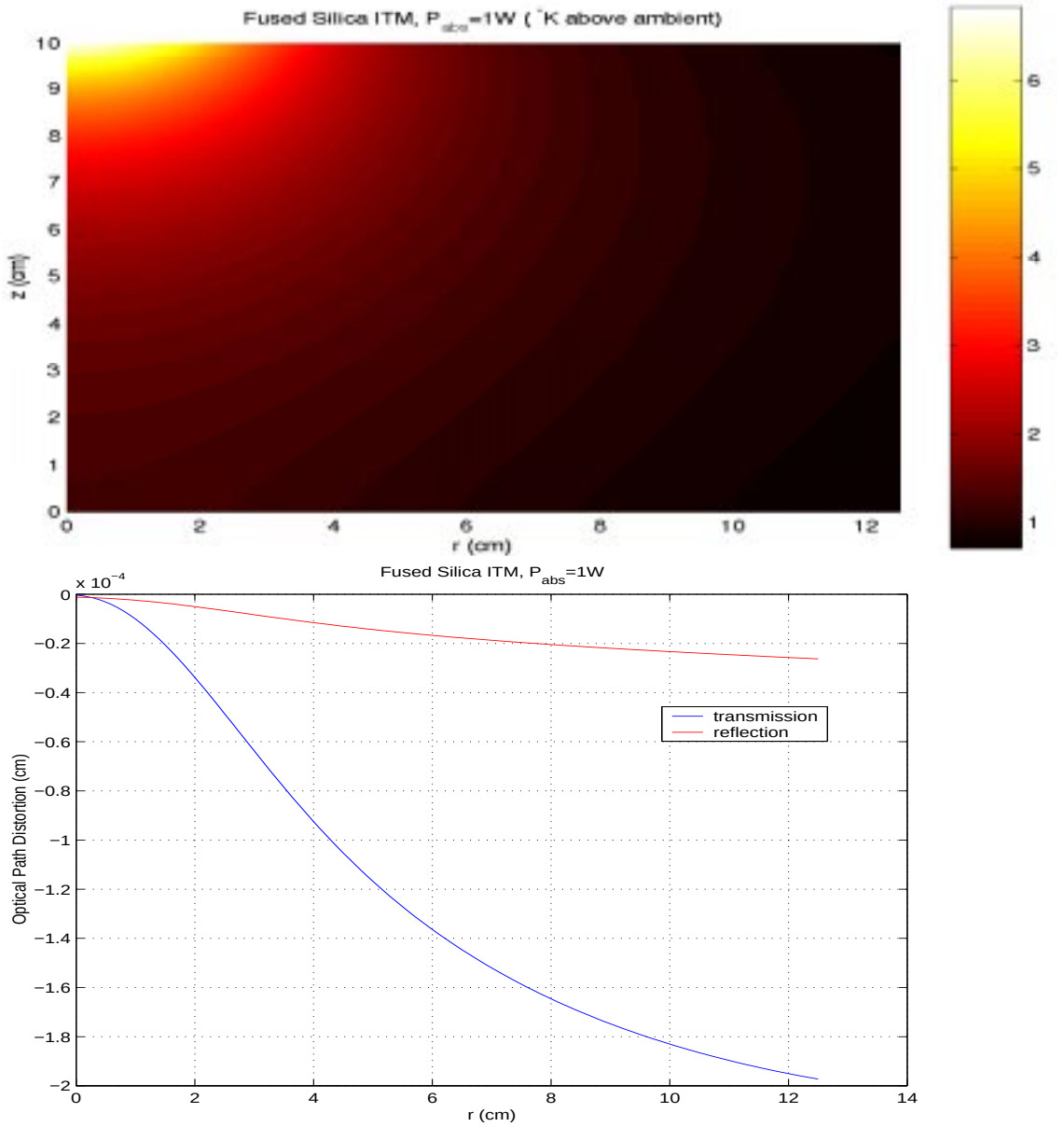

Figure 7: Calculated temperature field and resulting thermal lens for a fused silica LIGO II test mass. A total power of 1 Watt is absorbed, 95% on the Fabry-Perot surface, 5% in the bulk. The reflected optical path distortion is calculated for beams reflecting off of the Fabry-Perot surface.

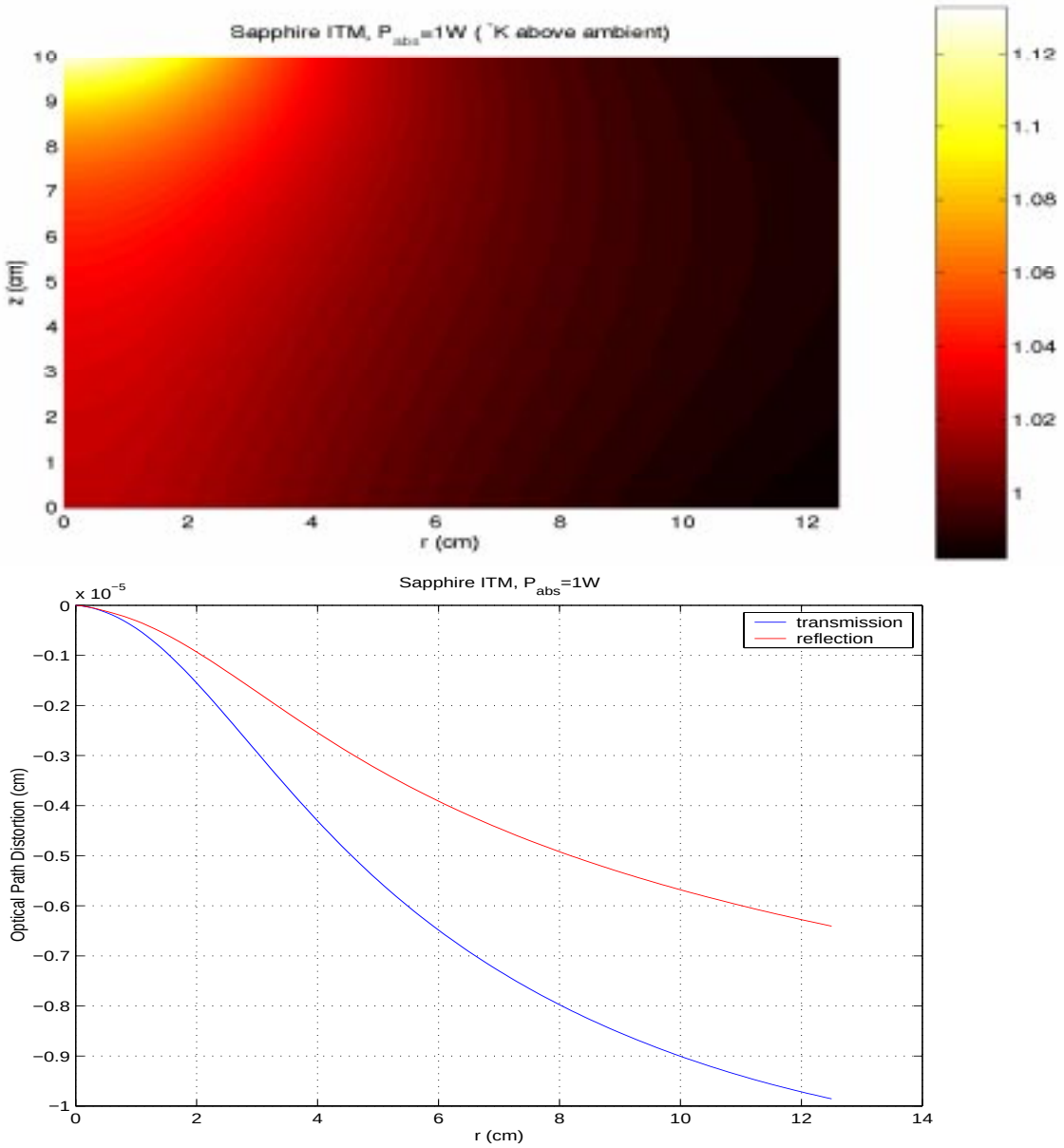

Figure 8: Calculated temperature field and resulting thermal lens for a sapphire LIGO II test mass. A total power of 1 Watt is absorbed, 50% on the Fabry-Perot surface, 50% in the bulk. The reflected optical path distortion is calculated for beams reflecting off of the Fabry-Perot surface.

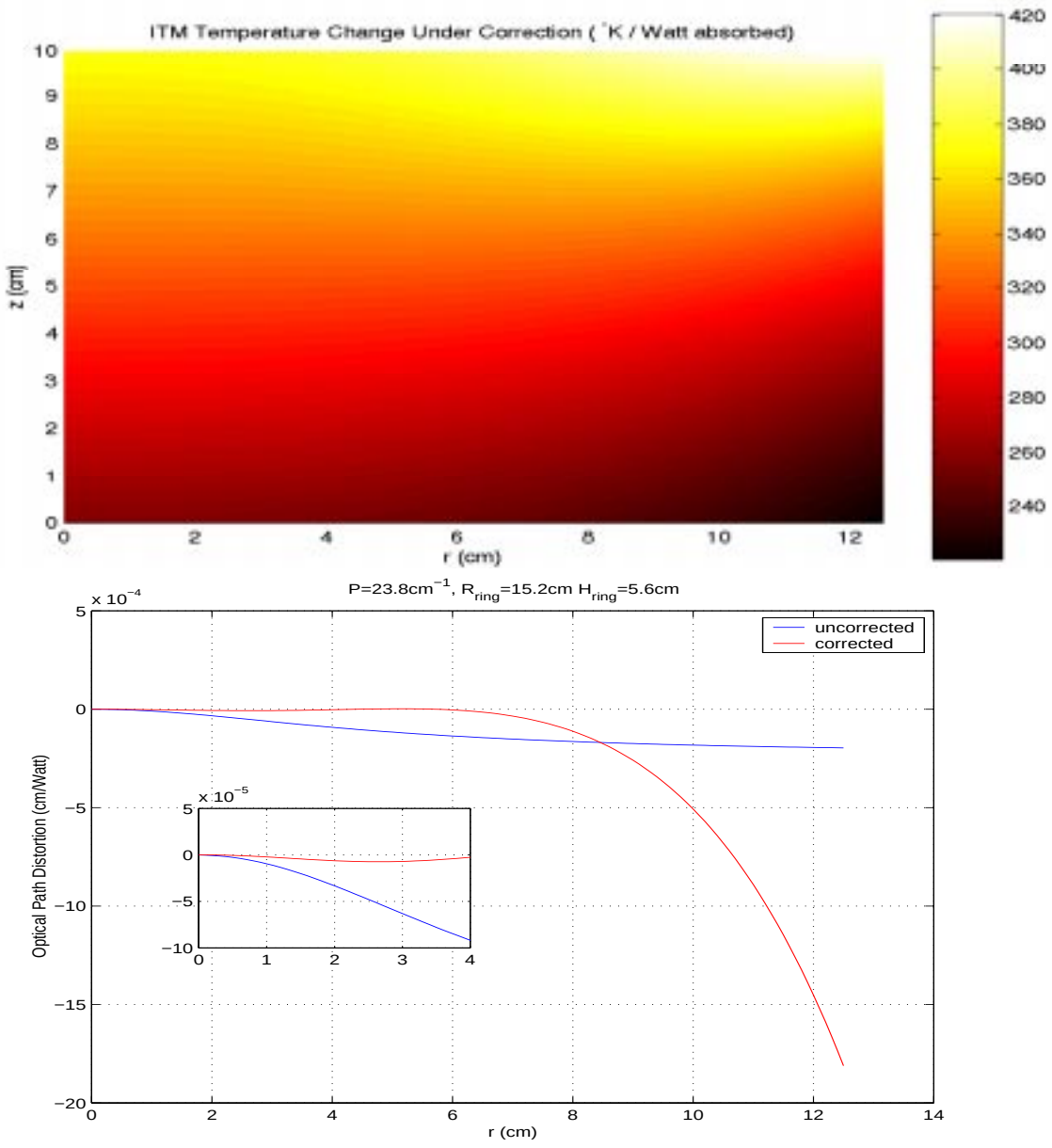

Figure 9: Optimal corrected temperature field and corresponding optical path distortion for a fused silica test mass under correction of a simple ring heater.

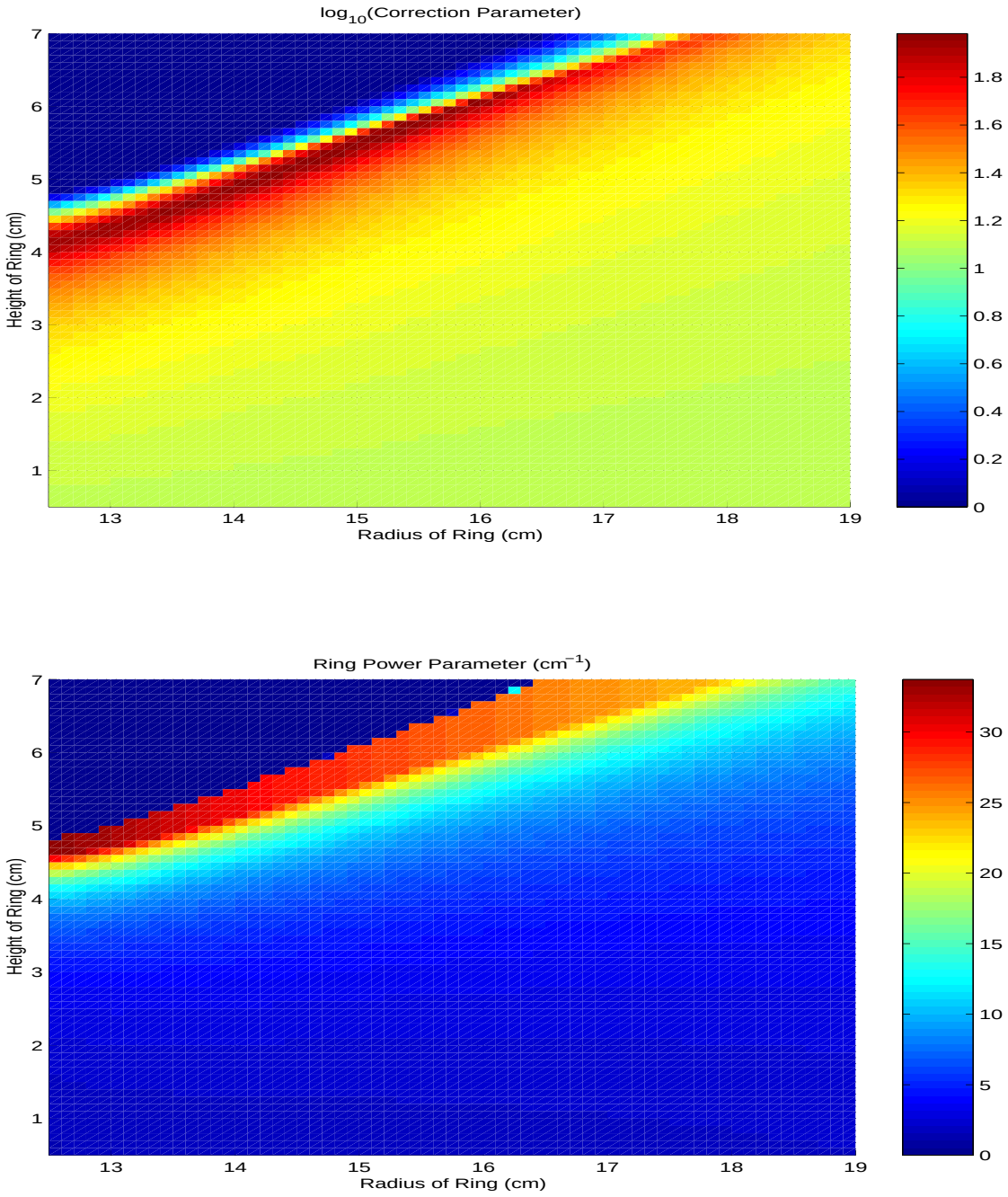

Figure 10: $\mathcal{C}$ maxized over P, and plotted over (R, h) for a fused silica test mass in LIGO II. The top diagram is the minimal value of $\mathcal{C}(R, h)$, and the bottom diagram is the ring power P required to attain the maximal value of $\mathcal{C}(R, h)$.

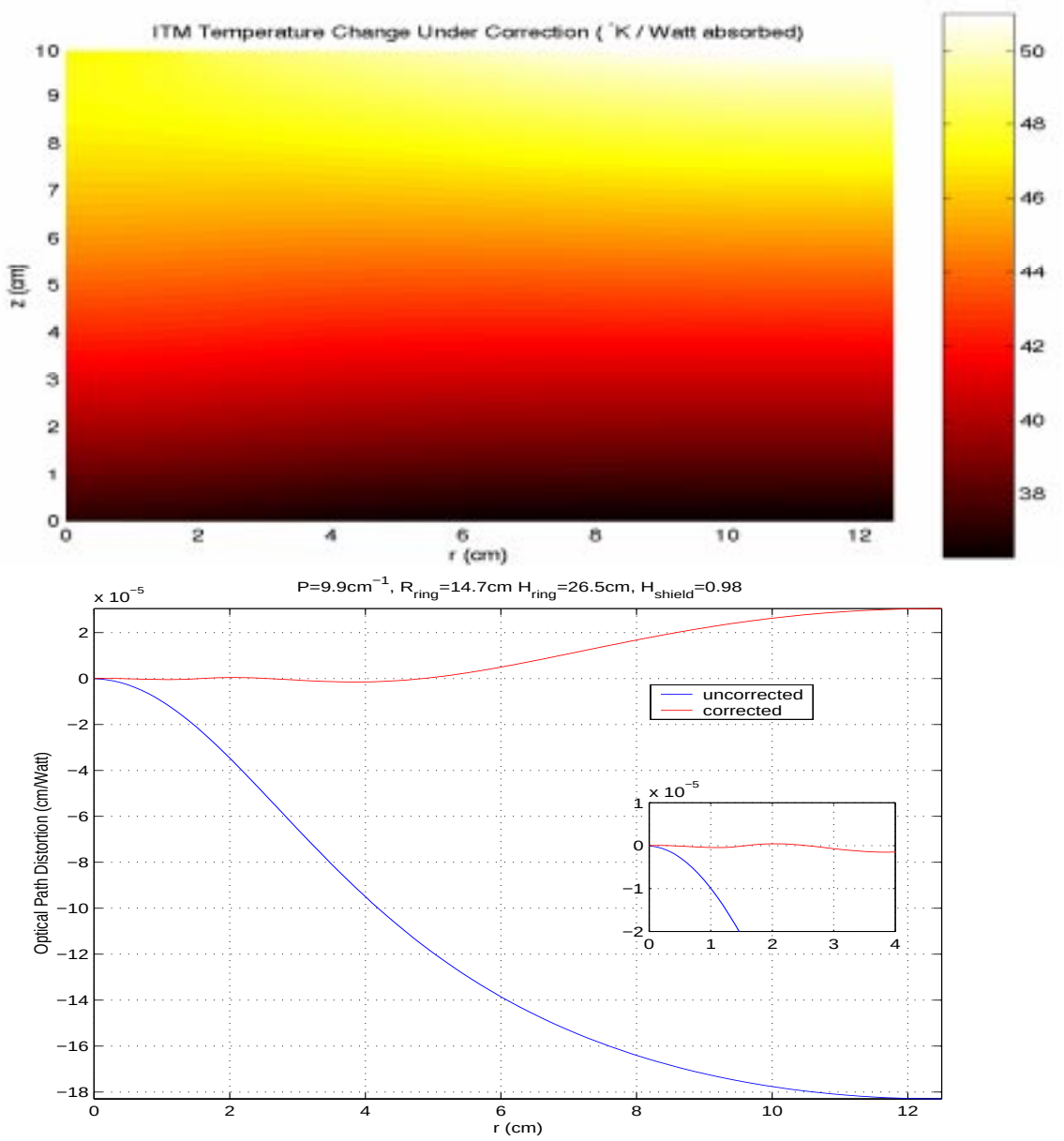

Figure 11: Typical corrected temperature field and corresponding optical path distortion for an insulated fused silica test mass under correction of a shielded ring heater.

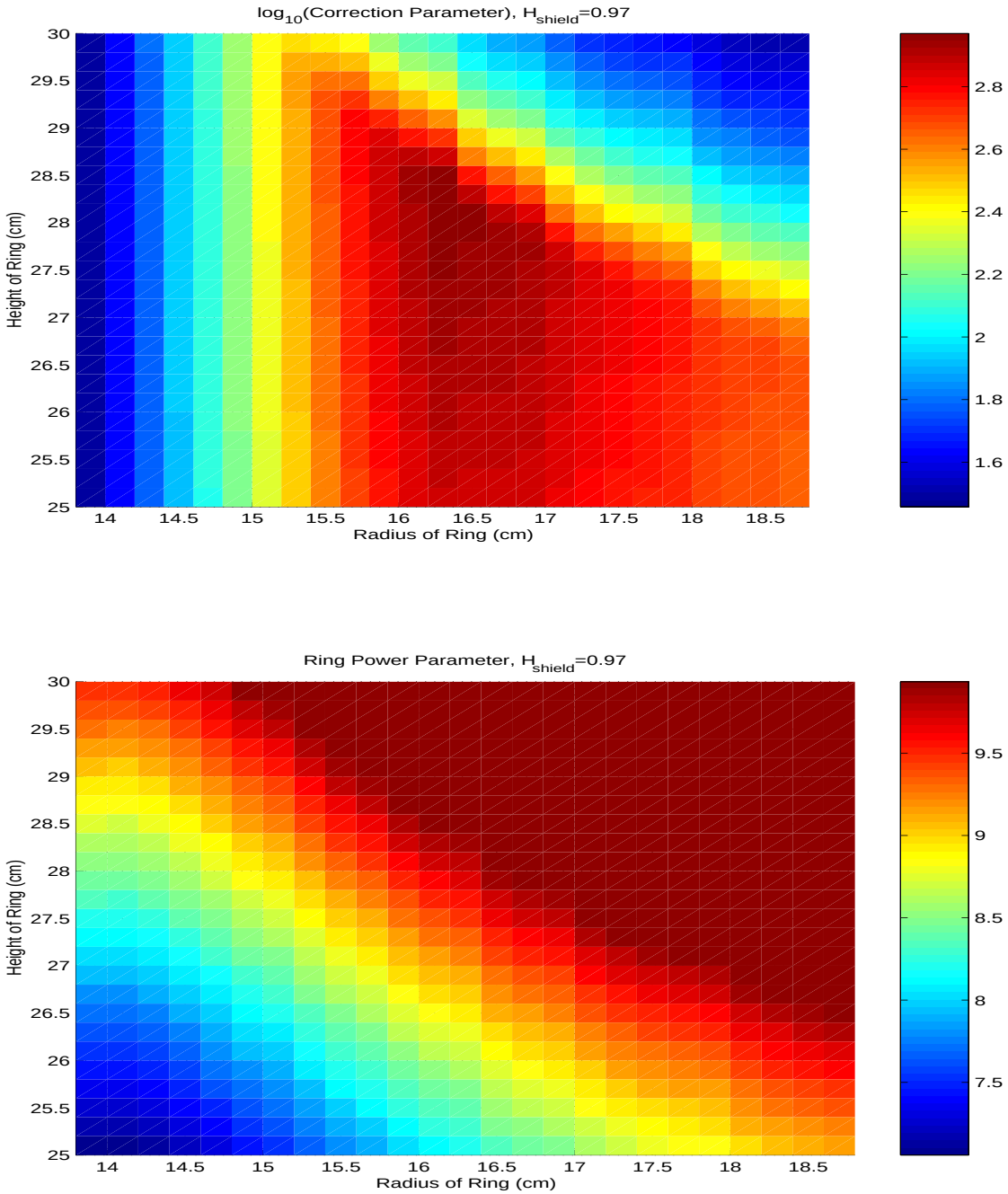

Figure 12: $\mathcal{C}$ maximized over P for a fixed shield height h', and plotted over (h, R) for a fused silica test mass in LIGO II. The top diagram is the minimal value of $\mathcal{C}(R, h)$, and the bottom diagram is the ring power P required to attain the maximal value of $\mathcal{C}(R, h)$

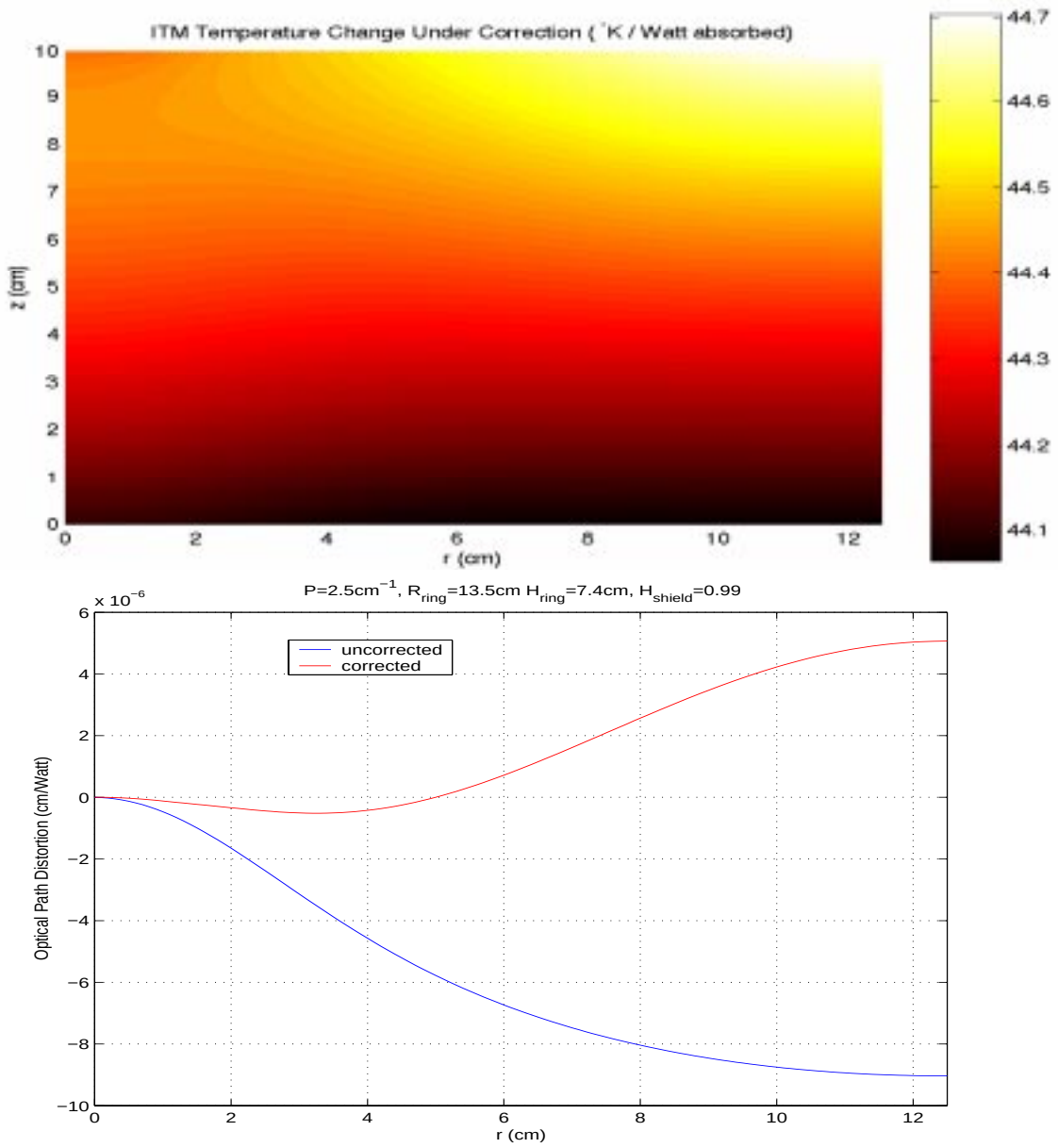

Figure 13: Optimal corrected temperature field and corresponding optical path distortion for an insulated sapphire test mass under correction of a shielded ring heater constrained to radiate a power $P \leq 130W$.

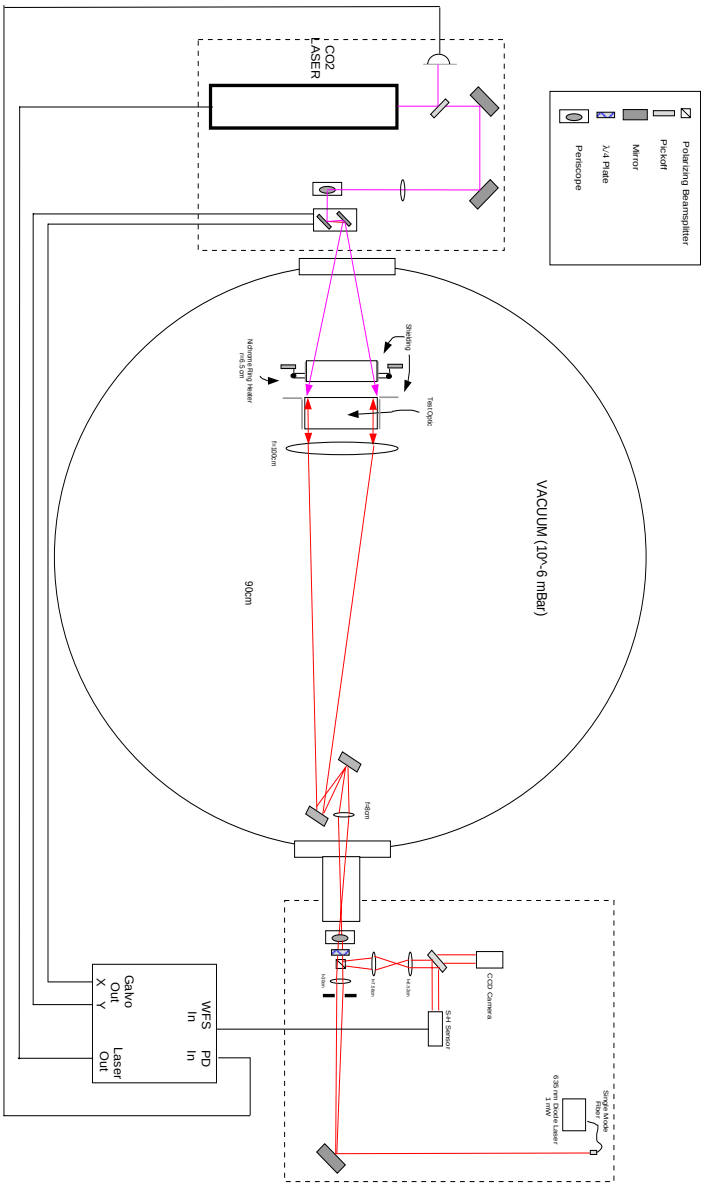

Figure 14: Diagram of the experimental apparatus constructed to demonstrate both schemes of thermal compensation.

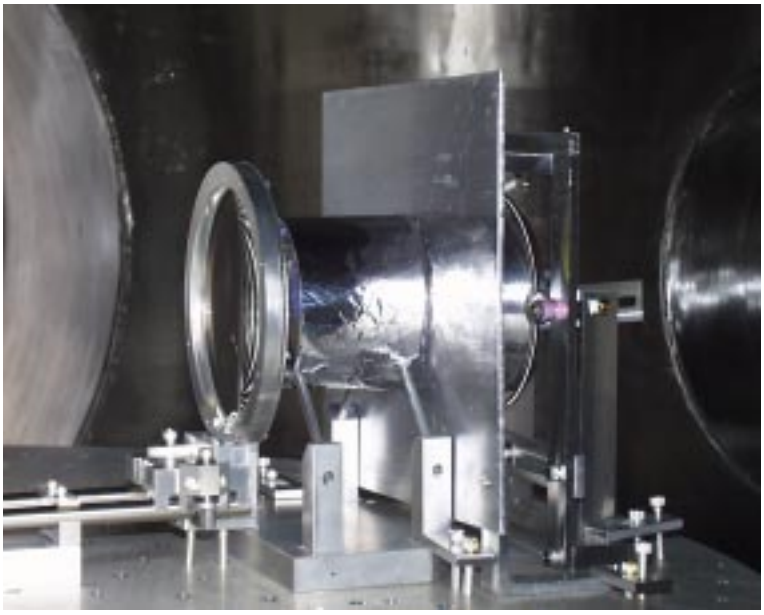

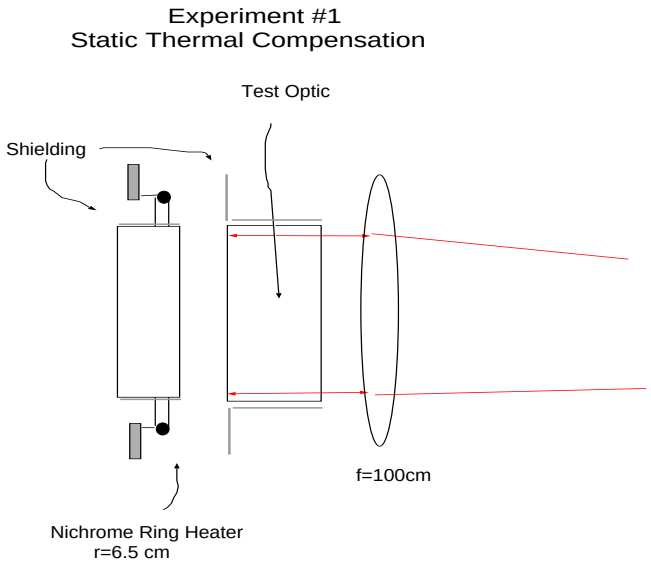

Figure 15: Photograph of the test optic in the experimental setup and a schematic diagram.

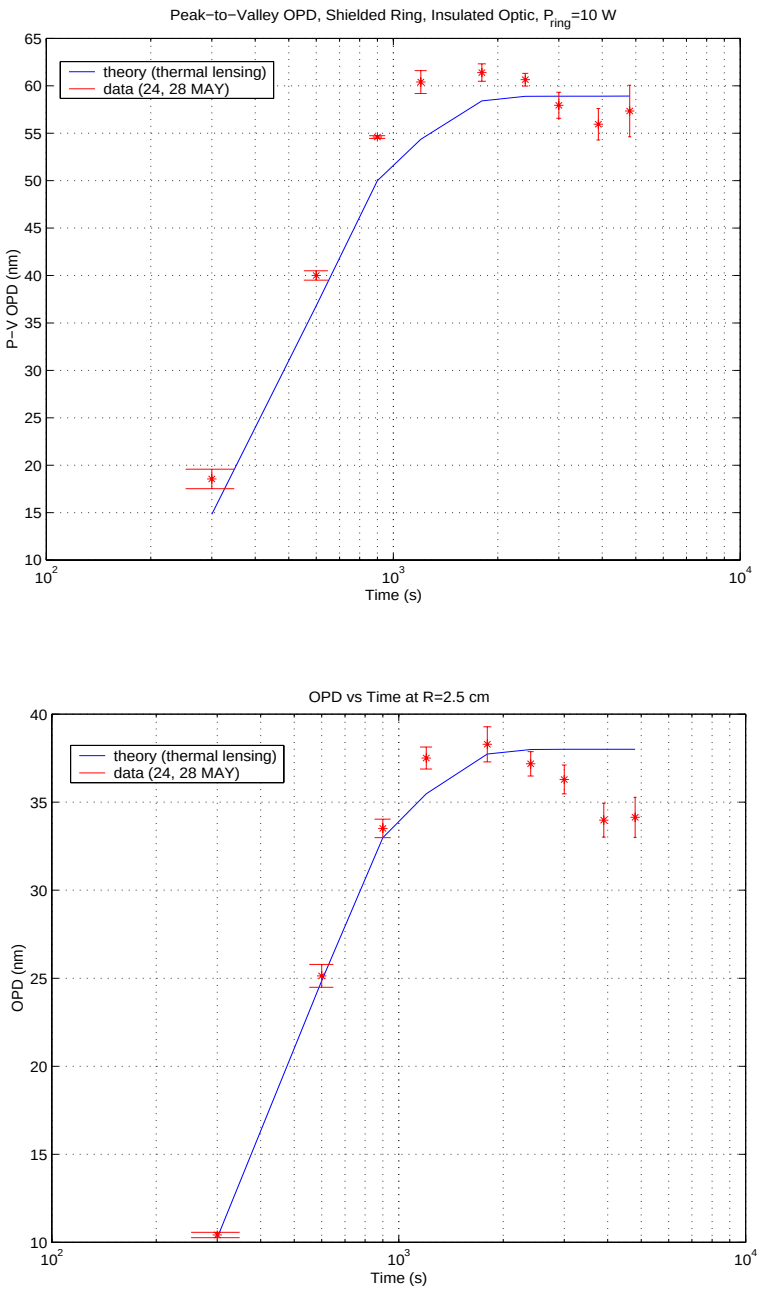

Figure 16: Measured optical path distortion vs. time taken at radii 2.5 cm and 4 cm for an insulated fused silica optic under actuation by a shielded heating ring.

References

[1] Hello P. and Vinet J., Analytical models of transient thermoelastic deformations of mirrors heated by high power cw laser beams, *J. Phys. France* **51** (1990) 2243-2261

[2] Lide, David R., Ed., *CRC Handbook of Chemistry and Physics, 71st Edition*. CRC Press (Boca Raton, FL 1990) pp. 4-41, 4-100, 5-17, and 5-49.

[3] Tapping J. and Reilly ML., Index of sapphire between 24 and 1060 degrees C for wavelengths of 633 and 799 nm, *J. Opt. Soc. Am. A* **3** [5] (1986) 610-616

[4] Louden, Rodney *The Quantum Theory of Light*. Clarendon Press (Oxford, England 1973)

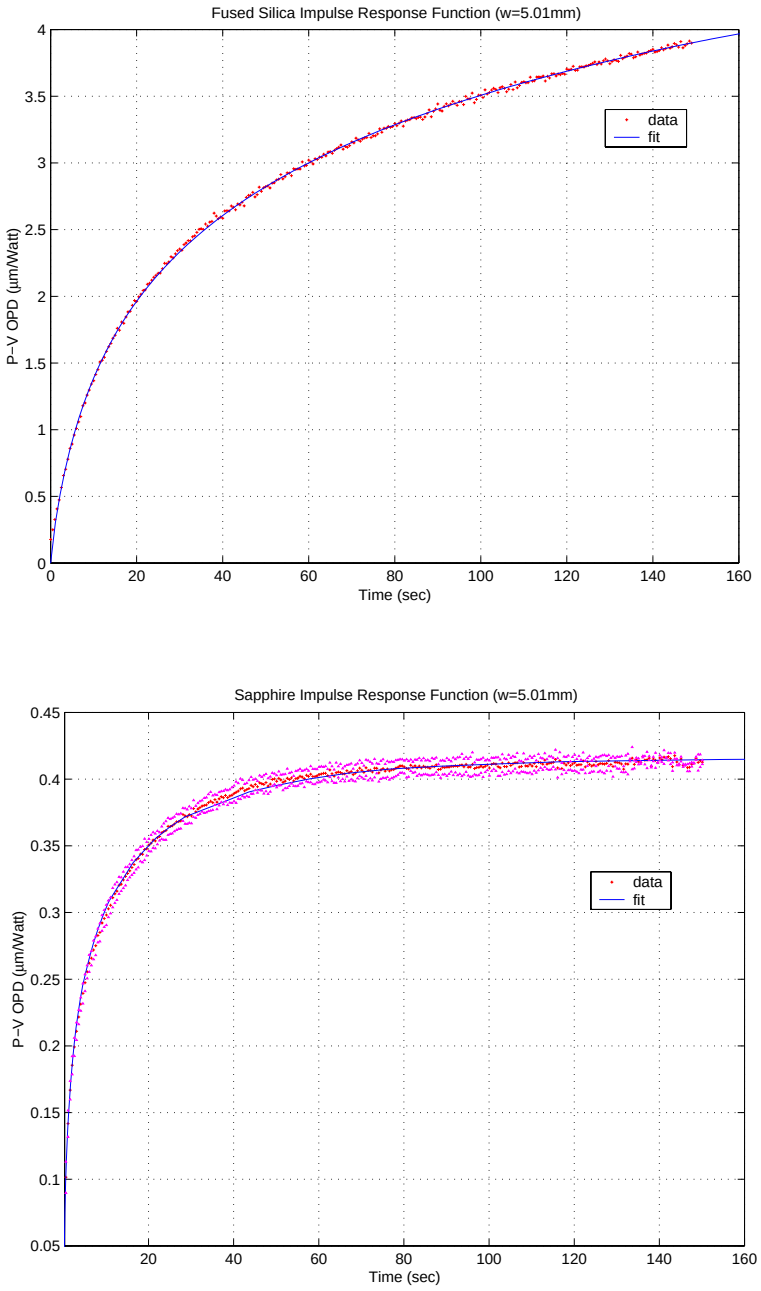

Figure 17: Measured peak to valley optical path distortion (transmission) per watt of power absorbed vs. time after onset for large fused silica (above) and large sapphire (below) test pieces.